THE JOURNAL OF PHYSICAL CHEMISTRY C
A JOURNAL OF THE AMERICAN CHEMICAL SOCIETY

pubs.acs.org/JPCC Article

Active Ag/Co Composite Chiral Nanohole Arrays

Hoang Mai Luong,* Minh Thien Pham, Tho Duc Nguyen, and Yiping Zhao

Cite This: J. Phys. Chem. C 2021, 125, 716–723

Read Online

ACCESS | Metrics & More | Article Recommendations | Supporting Information

ABSTRACT: The magneto-chiroptical properties of Ag/Co composite chiral nanohole arrays (CCNAs) are investigated. The intrinsic circular dichroism of CCNA samples was induced by in-plane symmetry breaking by a glancing angle deposition method, and it can be enhanced strongly by surface plasmon resonance when Ag is a major component. On the other hand, the Co component allows for magnetic tuning circular dichroism, with the maximum modulation amplitude up to 0.35°. Remarkably, the enhanced local electric field induced by Wood's anomalies gives rise to sharper and stronger magnetic circular dichroism (normalized for the same Co content) of samples with high Ag concentration. The result demonstrates the possibility of fabricating large-scale active chiroptical metasurfaces using CCNAs, which is promising for imaging and sensing applications.

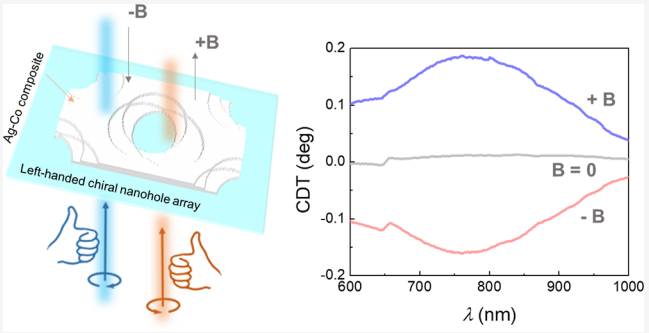

Downloaded via UNIV OF GEORGIA on April 1, 2021 at 00:54:36 (UTC).
See https://pubs.acs.org/sharingguidelines for options on how to legitimately share published articles.

1. INTRODUCTION

Recently, active chiral plasmonic metamaterials (CPMs) have attracted considerable attention.[1] In general, the optical response of the active CPMs has been tuned by an external stimulus such as light,[2−6] mechanical stretch,[7] temperature, electric field,[8−11] magnetic field,[12−15] and so on. Among all tuning mechanisms, magnetically switching optical chirality has been widely considered because of numerous advantages, such as ultrafast switching speed, continuous tunability, and easy integration and operation.[1,16] By incorporating a magnetic material into a CPM structure to form the so-called chiral magnetoplasmonic (CMP) metamaterial, one is able to tune the corresponding chiroptical properties by an external magnetic field due to the magneto-optical (MO) effect. Such an effect has been realized by a few structures, such as in multilayer Au/Co gammadion,[12] plasmonic chiral oligomers with a Au/Co multilayer,[14] Au/Co split ring,[15] Au/Ni trimer nanoantennas,[16] and so on. In these structures, when the MO-active material (Co, Ni, and Fe) is coupled with chiral plasmonic nanostructures, the strong local electromagnetic fields produced by the plasmonic material (Ag and Au) through the localized surface plasmon resonance (LSPR) interact strongly with the magnetic material.[17] Consequently, the MO and circular dichroism properties of the magnetic material could be significantly altered by the externally applied magnetic field.[17] So far, all the reported magnetically tuned CPMs are composed of ferromagnetic and noble metals in a two- or three-dimensional (2D and 3D) fashion, such as multilayer structures or separated antennas of single-component ferromagnetic/noble metals.[12,14−16] However, it is to be seen if an alternative material system that possesses both magnetic and plasmonic responses, such as a composite of noble metals and magnetic materials, that is, Au and Ag composites with Co, Fe, or Ni, will also be able to construct a good CMP structure. In fact, the use of composite materials in the MO nanostructure has recently been demonstrated by our group to enhance magnetoplasmonic performances of achiral nanostructures (such as nanohole arrays[18] or nanotriangle arrays[19]) in comparison to those made of pure ferromagnetic materials.

In this work, we propose to design, fabricate, and characterize a composite chiral nanohole array (CCNA) by a shadow sphere lithography technique (SSL) made from Ag and Co with different compositions.[20] Ag/Co vapors are co-evaporated with different polar/azimuthal angles, and the resulting CCNAs break the mirror symmetry in both in-plane and light propagation directions and induce strong intrinsic optical chirality. The Co content in CCNAs allows the magnetically tunable optical chirality, while the Ag component induces a strong surface plasmon polariton (SPP) and LSPR and further enhances the tunability of the chiral response. Finite-difference time domain (FDTD) calculations are performed to confirm the experimental results and to give an insight into optical chirality of CCNA structures and their compositions.

Received: September 3, 2020
Revised: December 15, 2020
Published: December 30, 2020

ACS Publications © 2020 American Chemical Society

https://dx.doi.org/10.1021/acs.jpcc.0c08057
J. Phys. Chem. C 2021, 125, 716−723

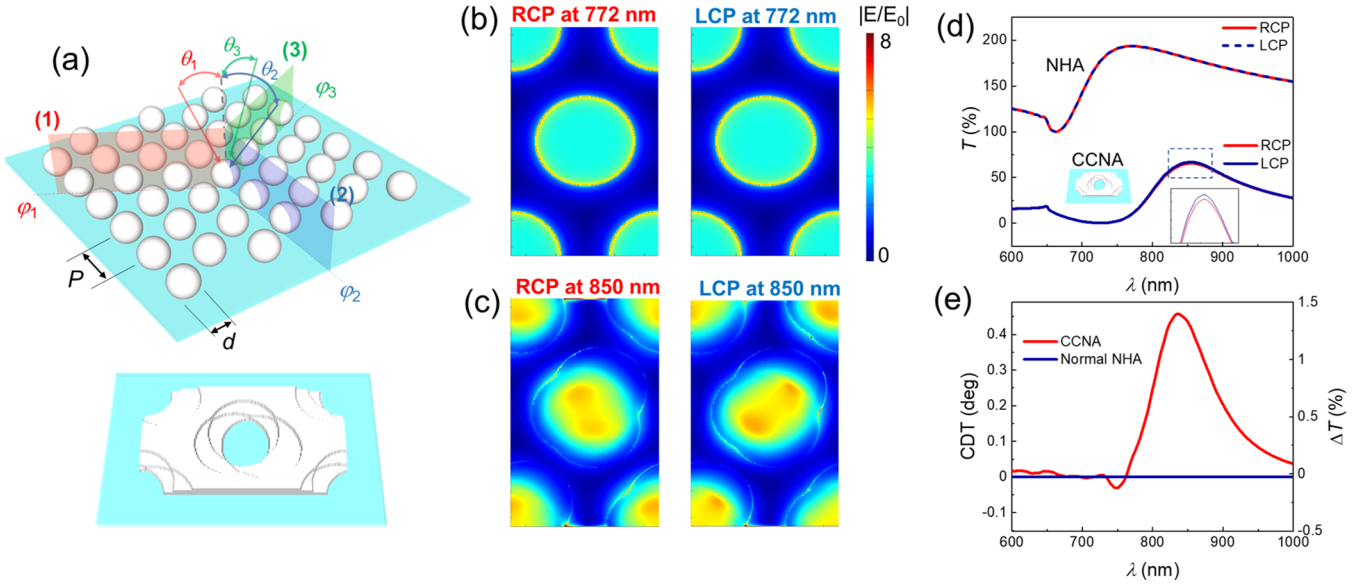

Figure 1. (a) Top panel: schematics of the fabrication process and the main parameters of polar angle θ, azimuthal angle φ, period P, and diameter of the etched sphere d. Bottom panel: Calculated structures of the LH-CCNAs based on an in-house MATLAB program. (b) FDTD-calculated electric field near a symmetric Ag nanohole array (NHA) illuminated with the RCP and LCP light at λ = 772 nm. (c) Calculated field distributions of Ag CCNA under illumination of RCP and LCP light at λ = 850 nm. (d) Calculated $T_R(\lambda)$ and $T_L(\lambda)$ of symmetry NHA and CCNA samples and (e) corresponding CDT spectra.

2. METHODS

Materials. Deionized water (18 MΩ.cm) was used for all experiments. Polystyrene (PS) nanospheres (Polysciences Inc., D = 500 nm) and ethanol (Sigma-Aldrich, 100%) were used to create the nanosphere monolayers. Silver (99.999%), cobalt (99.95%), and titanium (99.995%) obtained from Kurt. J Lesker Company were utilized for electron beam deposition.

PS Nanosphere Monolayer Preparation. The PS nanosphere monolayers were prepared by the air−water interface method, as previously reported.[21−24] The 0.01 % w/v solution of the PS nanosphere was washed several times by centrifugating and diluted with ethanol to a 2:1 volume ratio. The solution was then dispensed onto a petri dish (filled with 2 mm depth of water) at a rate of 0.009 mL/min. The monolayer slowly formed on the water surface as the process was carried on. After this process was over, the glass and Si substrates were carefully placed under the monolayer and the water level was lowered until dry. The achieved monolayer was then plasma-etched in a Trion Technology Phantom III RIE/ICP system to reduce the diameter of the nanosphere. In order to obtain a diameter of ∼350 nm, the etching was performed at a pressure of 40 mTorr with a 10 sccm oxygen flow, an ICP power of 25 W, and a radio frequency power of 10 W for 350 s.

Fabrication Processes. The monolayer-coated substrates were loaded into a custom-built dual-source electron deposition system (Pascal Technology) and mounted on a motor-controlled rotated holder. The metal depositions were performed when the base pressure of the chamber reached 10^{-6} Torr, and the working pressure of chamber during the deposition was kept under 5×10^{-6} Torr. A thin layer of Ti (t_{Ti} = 3 nm, deposition rate = 0.05 nm/s) was first coated in order to increase the adhesion between composite thin films and the substrates. A composite layer was then formed by depositing Ag and Co simultaneously. The vapors of Ag and Co came from two separate crucibles, which are about 0.5 m apart from the substrate holder. The thicknesses and deposition rates of Ag and Co were measured independently by two separated quartz crystal microbalances (QCMs). The total deposition rate was set to be 0.60 nm/s. The volumic ratio of Co (C_{Co}) in the Ag/Co composite thin film and CCNA was controlled by adjusting the deposition rate of Ag and Co, and a series of samples with different C_{Co} was fabricated [C_{Co} = 0, 30, 50, and 100 (% V)]. Afterward, the PS nanospheres were removed, and the substrates were subsequently washed with toluene, isopropyl alcohol, and deionized water to remove residual PS. Before any characterizations, the CCNA samples were stored inside a M. Braun glovebox system filled with N_2 (the concentrations of O_2 and H_2O are less than 0.1 ppm) to minimize potential oxidation effects.

Morphology and Composition Characterization. The morphologies of CCNAs were characterized by an atomic force microscope (Park NX10), and all the atomic force microscopy (AFM) images were analyzed by XEI—Image Processing and Analysis Software. The crystallinities of the composite materials were investigated by an X-ray diffractometry with a PANalytical X'Pert PRO MRD X-ray diffractometer at a fixed incident angle of 2.5°.

3. RESULTS AND DISCUSSIONS

The CCNAs are designed based on thin film-perforated nanohole arrays (NHAs), which have the following exclusive properties: (i) the extraordinary optical transmission (EOT) effect: the optical transmission in the plasmon-grating coupling wavelength region can be much greater than that predicted by Bethe's theory simply for light going through a single hole;[25] (ii) coexistence of SPP and LSPR which could be used to enhance the high chiro-optical and magneto-optical responses;[17] (iii) multifunctional properties (plasmonic and magneto-optical properties coexist in the system), which come from the Ag/Co composite material used;[18] and (iv) ultrathin thickness. The light−material interaction in this system can be optimized by many factors, such as the shape and dimension of the hole aperture, deposition symmetry, film thickness,

https://dx.doi.org/10.1021/acs.jpcc.0c08057
J. Phys. Chem. C 2021, 125, 716−723

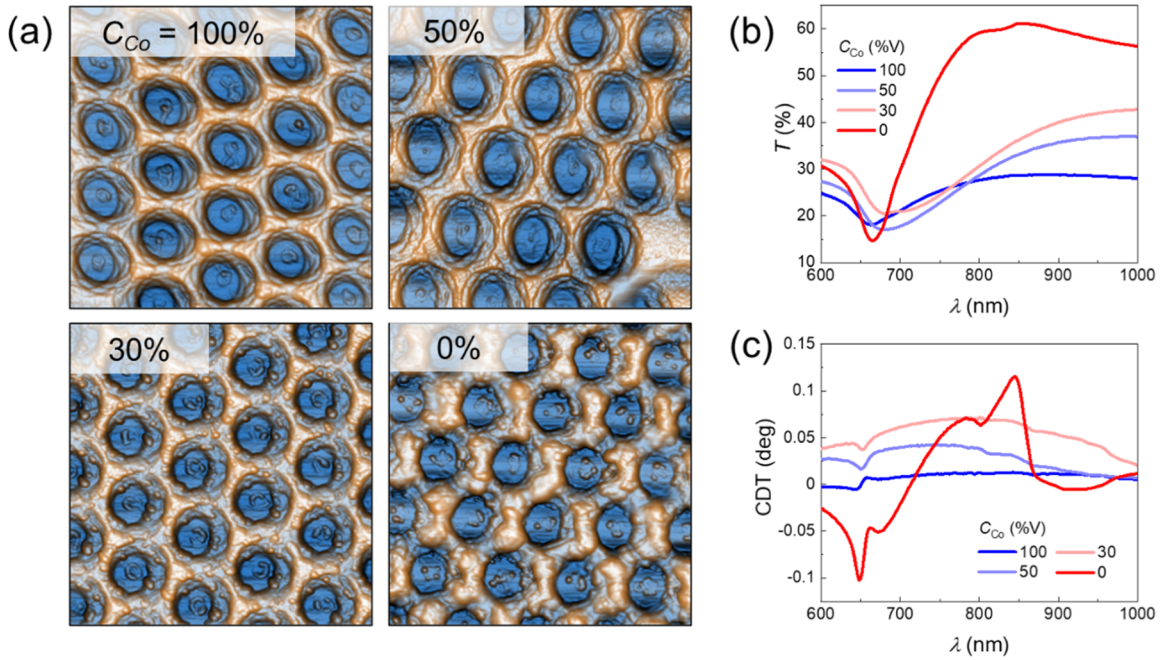

Figure 2. (a) Representative AFM images of CCNAs with different C_{Co} (% V). (b) Optical transmission spectra of CCNA samples, illuminated by unpolarized light. (c) CDT spectra of CCNA samples.

periodicity, lattice symmetry, filling factor of the NHA, composition of the materials, and so on in order to achieve maximum chiro-optical properties.[25] Nevertheless, the chiral responses can be magnetically tunable over a broad spectral range, which can potentially be used for ultrafast optical switch.[16] This large tunable parameter space makes the design of NHA-based CMPs more flexible. The proposed CCNA fabrication strategy by SSL is depicted in Figure 1a.[20] Hexagonal non-close-packed nanosphere (period P = 500 nm, diameter d = 350 nm) monolayers were used as a template. Ag and Co vapors were then simultaneously deposited at different incident and azimuthal angles for three consecutive depositions, $\theta_1 = 10°$ and $\varphi_1 = 0°$, $\theta_2 = 20°$ and $\varphi_2 = 120°$, and $\theta_3 = 30°$ and $\varphi_3 = 240°$, where θ_1, θ_2, and θ_3 were the vapor incident angles with respect to the substrate normal; φ_1, φ_2, and φ_3 were the relative projected azimuthal angles of incident vapor on the substrate plane. Note that these angles of θ and φ were chosen to minimize the domain effects to circular differential transmission (CDT) spectra.[20] During the three consecutive depositions, the ratio of the Ag and Co deposition rates, the deposited time, and thickness for each deposition were fixed as a constant. Note that the azimuthal rotation direction of the substrate for the three consecutive depositions was counter-clockwise, which resulted in a left-handed- (LH-) CCNAs, and yielded favorable optical transmission with left-circularly polarized light (LCP) (which will be discussed below).[20]

We first evaluate the chiroptical response of the Ag CCNA structure as well as achiral NHA by FDTD calculations, which were carried out using a commercial software (Lumerical FDTD Solutions).[26] The geometry parameters of achiral and chiral NHA structures were based on the surface morphology generated from a home-built MATLAB program (with period P = 500 nm, diameter d = 350 nm),[27,28] and the complex optical permittivity $\varepsilon = \varepsilon_1 + i\varepsilon_2$ of Ag used for calculations was extracted experimentally from the ellipsometry data of the corresponding thin films.[18] Two separated calculations with left-(LCP) and right-circularly polarized light (RCP) were performed, and the difference between the optical transmission in two cases was obtained. In addition, the electric field distributions at a certain cross section were taken by a frequency-domain field and power monitor. The near-field electric field distributions at EOT wavelength position of achiral NHA and CCNA samples (extracted at the Ag−air interface) is summarized in Figure 1b,c, respectively. While the achiral NHA shows no difference in near-field electric field distribution when it is excited with LCP and RCP (Figure 1b), CCNA exhibits noticeable differences in electric field distribution when it is illuminated with LCP and RCP (Figure 1c). As a result, the optical transmission at the far field also exhibits different optical responses: while the LCP and RCP optical transmissions of achiral NHA are identical, those of CCNA show discrepancies at the transmission dip ($\lambda \approx 750$ nm) and EOT peak ($\lambda_{EOT} \approx 850$ nm) (Figure 1d,e). We highlight that the large chiral optical transmission response is frequently desired to be associated with large optical transmission, which is the case at the EOT peak. In addition, the differences between the peak and dip positions of optical transmission spectra (Figure 1d) come from a larger effective hole volume of CCNA in comparison to that of achiral NHA. The red shifts of these dips/peaks are consistent with the previous works.[29,30]

Figure 2a shows the representative AFM images of LH-CCNAs with different Co concentrations C_{Co} = 100, 50, 30, and 0 of volume percentage (% V) (which is referred to as $CCNA_x$, where x = 100, 50, 30, 0, respectively). The thicknesses of the films are consistent at about 55 ± 7 nm, which matches the morphology simulated from an in-home MATLAB program.[27,28] The nonpolarized optical transmission spectra of the CCNAs are shown in Figure 2b. In general, the shape of spectra is similar regardless of C_{Co}, with a transmission maximum peak at $\lambda_{peak} \approx 850$ nm and a local minimum at $\lambda_{dip} \approx 660$ nm (the spectra with a wider wavelength range can be found in Figure S2a). Based on the

https://dx.doi.org/10.1021/acs.jpcc.0c08057
J. Phys. Chem. C 2021, 125, 716−723

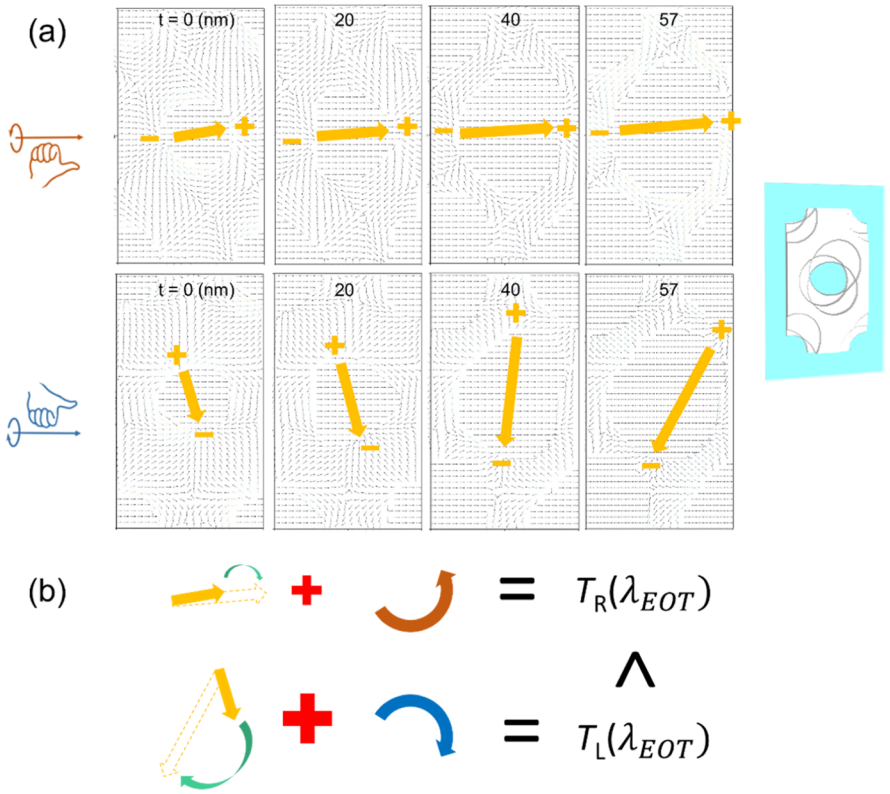

Figure 3. (a) Local current density distributions of the $CCNA_0$ sample excited by a RCP (top panel) and a LCP (bottom panel) incident light at λ_1 = 850 nm for the plane t = 0, 20, 40, and 57 nm respectively. The arrows indicate the current density direction. (b) Top-view illustration of rotations of effective current pole directions from the top layer to the bottom layer under RCP and LCP illuminations, respectively. The straight dashed arrows represent the pole direction at the t = 0 nm plane, while the solid arrows show the pole direction at the t = 57 nm plane.

Bloch wave condition and Wood−Rayleigh anomaly condition, we assigned the transmission maximum $\lambda_{peak} \approx 850$ nm and a local minimum at $\lambda_{dip} \approx 660$ nm as the (1,0) resonance mode and (1,0) Wood's anomaly at the film−glass interface, respectively (more details can be found in Section S2 in Supporting Information). The wavelength positions of λ_{peak} and λ_{dip} as a function of C_{Co} are summarized in Figure S2b. λ_{dip} shows an insignificant change when C_{Co} increases, which agrees well with the Wood−Rayleigh anomaly theory because Wood's anomalies are purely geometric and the corresponding wavelength position does not depend on the optical permittivity and plasmonic properties of the metal film, as stated in eq S2 in Supporting Information.[31] On the other hand, λ_{peak} shows a larger change on C_{Co}, as this peak is sensitive to the film permittivity (ε_d, as seen in eq S1 in Supporting Information) and other geometrical parameters (such as film thickness,[32,33] hole diameter,[33] and hole shape[34]).

Figure 2c shows the CDT spectra [CDT (deg) = 32.98° × $(T_{LCP} - T_{RCP})$][35−37] of the CCNA sample with different C_{Co}. As expected, $CCNA_0$ gives the strongest CDT signal, with a peak at $\lambda \approx 850$ nm and a dip at $\lambda \approx 650$ nm. We note that the CDT spectra for different azimuthal angles and illumination directions show good resemblances, which implies that the majority of the signal originates from the chirality instead of linear anisotropy (Section S3 in Supporting Information). As C_{Co} increases, the magnitude of CDT at these extrema wavelengths decreases and is about a magnitude of order smaller when C_{Co} = 100 % V, and the spectral feature becomes very broad. This observation can be explained by the strong local electric fields induced by plasmon resonance in the $CCNA_0$ sample (Figure S5 in Supporting Information).[18] When C_{Co} increases from 0 to 50% V, the imaginary part ε_2 of optical permittivity of composite film increases, while the real part ε_1 of optical permittivity becomes less negative and approaches to that of the pure Co,[18] which dampens the SPR and reduces the CDT at the resonance wavelengths. In addition, the majority of the CDT signal of the $CCNA_{100}$ sample originates from the CCNA structure, that is, the symmetry breaking of the structure. More discussions about the effects of the structures and materials on the optical transmission and CDT responses can be found in Section S2 in Supporting Information.

In order to understand the chiro-optical response of the CCNA at the EOT, we underline the transmitting mechanism of optical field through the NHA structure. Unlike in the metal thin film where the electromagnetic waves must penetrate directly through the film and the evanescent field falls off exponentially from the surface, the introduction of NHA structure compensates the momentum mismatch between a free-space photon and a surface plasmon (SP) wave.[25] This additional quasi-momentum provided by NHA allows the SP to (i) be excited at the light incident film−dielectric interface, (ii) propagate on this interface (so called SPP), (iii) pass through the hole, and (iv) emit at the another film−dielectric interface and can be probed at the far-field (as illustrated in Figure S6 in Supporting Information).[38,39] Thus, any disparities of handedness structure that are involved in the processes (i−iv) can create a change in the optical transmission of circularly polarized light.

https://dx.doi.org/10.1021/acs.jpcc.0c08057
J. Phys. Chem. C 2021, 125, 716−723

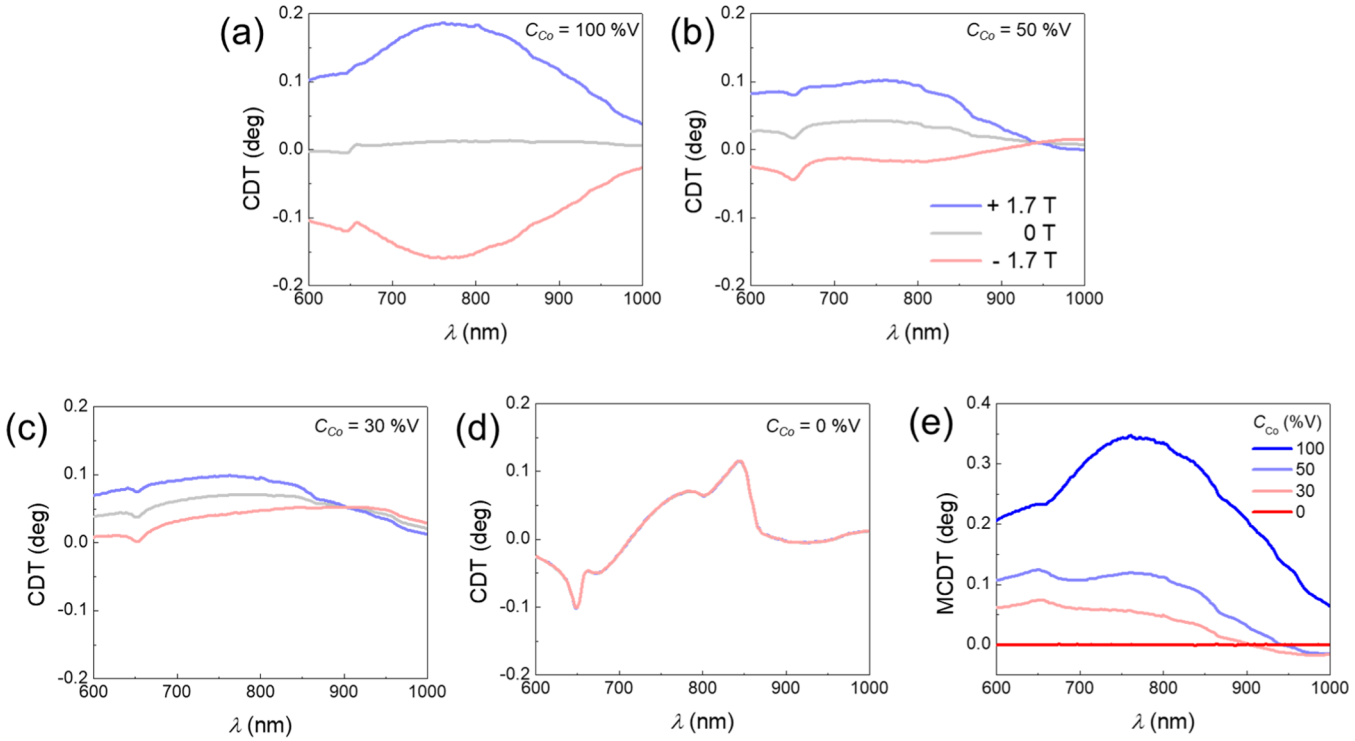

Figure 4. CDT spectra of CCNA samples under external magnetic field of $B = \pm 1.7$ T, with C_{Co} = (a) 100, (b) 50, (c) 30, and (d) 0 (% V), respectively. (e) MCD spectra of CCNA samples with different C_{Co}.

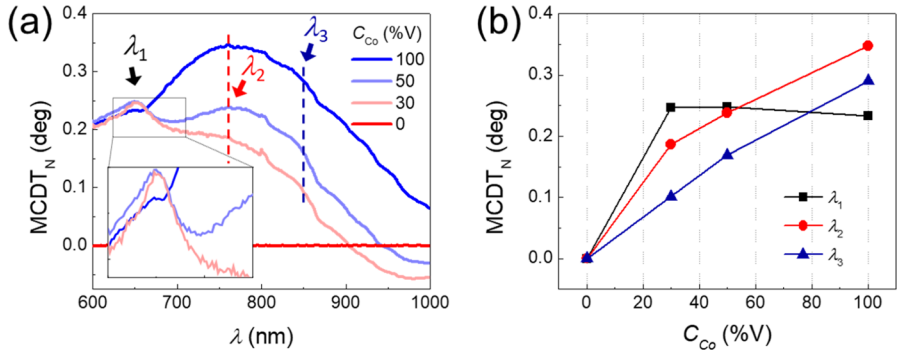

Figure 5. (a) Normalized $MCDT_N$ spectra of CCNA samples under external magnetic field of $B = \pm 1.7$ T, with different C_{Co}. (b) Plots of the $MCDT_N$ magnitudes of different CCNA samples extracted at λ_1, λ_2, and λ_3 vs C_{Co}.

Similarly, in our CCNA structure, SPPs on the light incident interface couple evanescently to the light-transmitted interface before being re-emitted into the far field. The role of SPPs is to enhance the electric field magnitude around the apertures and compensate for the exponential attenuation of the evanescent field in the depth of the nonpropagating aperture. Based on this knowledge, we hypothesize that the symmetric/dissymmetric coupling between the handedness of the chiral aperture and polarization of the electromagnetic wave in process (iii) originates the chiro-optical responses of the CCNA structure. In order to illustrate this point, the current densities of LH-$CCNA_0$ at different cross-section planes (excited from the glass−side interface by LCP and RCP at $\lambda \approx 850$ nm) were calculated by FDTD based on the structure exported from the AFM image, at thickness $t = 0$ (glass−film interface), 20, 40, and 57 nm (air−film interface), respectively (Figure 3a). In each cross-section plane, the current sources (i.e., negative and positive poles) were observable and the corresponding direction of the dipole changes with the propagation of the light. The orientations of these dipoles are summarized in Figure 3b. Under an RCP illumination, the dipole direction rotates about 5° clockwise along the light propagation direction. As the current dipole rotation is against the polarization rotation of the excited light, the dissymmetric coupling between the handedness of the aperture and polarization; that is, the opposite rotation would weaken the evanescent field and in turn reduce the transmission.[20,36] On the other hand, under an LCP illumination, the dipole orientation rotates 32° clockwise. In this case, the handedness of the structure is the same as the direction of the polarization. Thus, the evanescent field is supported and leads to a slightly higher transmission.[20] Another CDT extremum emerges at $\lambda \approx$ 650 nm, which is induced by the (1,1) resonance mode at film−glass interface in the $CCNA_0$ sample, and can be explained in a similar manner (Figure S7 in Supporting Information).

The effect of an external magnetic field to switch the optical chirality of the CCNA samples is shown in Figure 4 by

https://dx.doi.org/10.1021/acs.jpcc.0c08057
J. Phys. Chem. C 2021, 125, 716−723

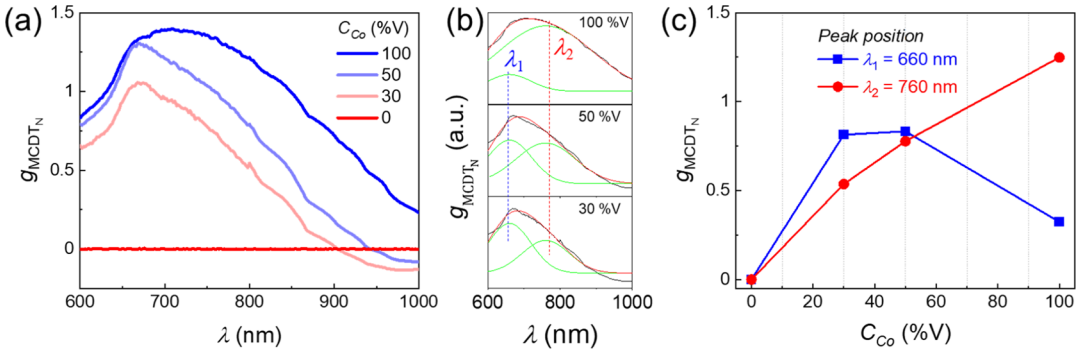

Figure 6. (a) g_{MCDT_N} spectra of Co CCNA with different C_{Co} and (b) fitting of these spectra with two peaks at λ_1 and λ_2. (c) Plots of the g_{MCDT_N} magnitudes of peak λ_1 and λ_2 in (b), as a function of C_{Co}.

applying a constant magnetic field, B = + 1.7 T, 0 T, and −1.7 T for CCNAs with different C_{Co}. Note that the normal angle of incidence of light was used and polar magnetic field was applied. Generally, the changes of CDT under the external magnetic field are the largest in a pure Co sample, and the magnitude of the change reduces gradually when C_{Co} decreases and reaches zero in a pure Ag CCNA sample. In addition, over the wavelength range of 600−900 nm, CDT increases when the direction of magnetic field lines is parallel with the wave vector of incident beam, and vice versa, CDT decreases when the direction of magnetic field lines is anti-parallel with the wave vector of incident beam. We note that this behavior of CDT under an external magnetic field might be different in other probing wavelength ranges (see Section S6 in Supporting Information). In order to quantitatively measure the change of CDT under magnetic field, we utilize the magnetic CDT (MCDT), which is determined by the following equation[40]

$$\mathrm{MCDT} = \mathrm{CDT}(+B) - \mathrm{CDT}(-B)$$

where the CDT($\pm B$) is the CDT signal measured at an external magnetic field of B = ± 1.7 T. Figure 4e shows the MCDT spectra extracted from Figure 4a−d, which reveal the largest MCDT magnitude for the pure Co CCNA sample, which decreases to null when C_{Co} decreases to 0 % V.

In order to compare the MCDT magnitude with different C_{Co}, we normalize MCDT for an amount of magnetic material, $\mathrm{MCDT_N} = (\mathrm{MCDT} \times 100)/C_{Co}$. The normalized $\mathrm{MCDT_N}$ spectra of CCNAs with different C_{Co} are summarized in Figure 5a. At C_{Co} = 100 % V (pure Co sample), CCNA shows the maximum CDT modulation magnitude ($\mathrm{MCDT_{100}}$) of ∼0.35° at $\lambda \approx 750$ nm. This modulation amplitude is in the same order of magnitude with up-to-date magneto-chiroptical devices.[12−15,40] As C_{Co} decreases, the magnitude of MCDT at this peak decreases in almost a linear fashion to null (as in the pure Ag CCNA sample, see Figure 4e). However, at $\lambda_1 \approx 660$ nm, there appears a peak. To gain a quantitative understanding, the magnitude of $\mathrm{MCDT_N}$ at two local peaks at $\lambda_1 \approx 660$ nm and $\lambda_2 \approx 760$ nm as well as at the EOT wavelength $\lambda_3 \approx 850$ nm are plotted as a function of C_{Co} in Figure 5b. While the magnitudes of $\mathrm{MCDT_N}$ at $\lambda_2 \approx 760$ nm and $\lambda_3 \approx 850$ nm decrease gradually when C_{Co} decreases, they behave differently at Wood's anomaly. At λ_1, the $\mathrm{CCNA_{30}}$ and $\mathrm{CCNA_{50}}$ samples yield an even higher $\mathrm{MCDT_N}$ than that of the $\mathrm{CCNA_{100}}$ sample. This peak also appears to be sharper with higher concentration of Ag, as can be seen in the inset of Figure 5a, which is consistent with our previous reports on the enhanced Faraday rotation at the plasmonic resonance.[41] The different behaviors at λ_1 can be explained by the enhancement of local electric field because of Wood's anomaly in comparison to that of the $\mathrm{CCNA_{100}}$ sample, which comes from the samples with a high ratio of Ag component (>50 % V) (Figure S1 in Supporting Information).

We further obtained the normalized asymmetry factor g_{MCDT_N} of the CCNA sample, which was calculated by the following equation

$$g_{MCDT_N} = \frac{g_{MCDT}}{C_{Co}} \times 100 = \frac{1}{C_{Co}} \frac{\mathrm{CDT}(+B) - \mathrm{CDT}(-B)}{T_{unpolarized}} \times 100$$

where CDT($\pm B$) is the CDT signal measured at an external magnetic field of B, $T_{unpolarized}$ is the unpolarized optical transmission, and C_{Co} (% V) is the volume concentration of Co. The obtained g_{MCDT_N} spectra for different C_{Co} are presented in Figure 6a. For the $\mathrm{CCNA_{100}}$ sample, a broad g_{MCDT_N} peak at $\lambda \approx 710$ nm is observed, as this peak is a combination of two peaks: the intrinsic $\mathrm{MCDT_N}$ peak at $\lambda_2 \approx 760$ nm and the peak raised by the low transmission ($T_{unpolarized}$) at Wood's anomaly $\lambda_1 \approx 660$ nm. As the composition of Ag is increased and C_{Co} = 50 % V, the magnitude of the peak at $\lambda_2 \approx 760$ nm decreases and the peak at $\lambda_1 \approx 660$ nm emerges with an unchanged magnitude in comparison to that of the $\mathrm{CCNA_{100}}$ sample. However, the magnitude of the g_{MCDT_N} peak at $\lambda_1 \approx 660$ nm further drops in $\mathrm{CCNA_{30}}$. In order to quantitatively evaluate the attribution of two peaks at λ_1 and λ_2 to the g_{MCDT_N} spectra with different C_{Co}, the broad peak is deconvoluted into two Gaussian peaks at λ_1 and λ_2, as presented in Figure 6b. The magnitude of peak λ_2, summarized in Figure 6c, increases almost linearly with C_{Co}, which is due to the intrinsic MO response of the added Co component. On the other hand, the g_{MCDT_N} magnitudes at peak λ_1 of $\mathrm{CCNA_{50}}$ and $\mathrm{CCNA_{30}}$ samples are larger than that of the $\mathrm{CCNA_{100}}$ sample. The anomaly in the behavior of peak λ_1 can be ascribed to the plasmonic enhancement effect induced by Wood's anomalies at λ_1. By compromising the C_{Co}, one can readily tune the intrinsic CDT signal as well as the magnitude of the MCDT signal of the CCNA sample.

4. CONCLUSIONS

In summary, we report the optical and magneto-optic chiropticality of the CCNA sample made from a low-cost

https://dx.doi.org/10.1021/acs.jpcc.0c08057
J. Phys. Chem. C 2021, 125, 716−723

SSL technique and electron beam metal codeposition. The CCNA sample shows a strong intrinsic CDT signal, which emerges at the optical resonance induced by SPR. This CDT signal can be modulated magnetically by an external magnetic field, with the modulation amplitude up to 0.35°. This result demonstrates the possibility of fabricating large-scale active chiro-optical metasurfaces using a CCNA sample, which is promising for imaging and sensing applications.

■ ASSOCIATED CONTENT

Supporting Information

The Supporting Information is available free of charge at https://pubs.acs.org/doi/10.1021/acs.jpcc.0c08057.

X-ray diffraction profiles of the Ag/Co composite thin film, effects of the structures and materials on the optical transmissions and CDTs; determination of linear artifacts in CDT measurements; time-averaged local E-field maps calculated by FDTD; and interaction between light and CCNAs (PDF)

■ AUTHOR INFORMATION

Corresponding Author

Hoang Mai Luong − *Department of Physics and Astronomy, University of Georgia, Athens, Georgia 30602, United States;* orcid.org/0000-0002-7792-4274; Phone: 706/542-8787; Email: hoanglm@uga.edu; Fax: 706/542-2492

Authors

Minh Thien Pham − *Department of Physics and Astronomy, University of Georgia, Athens, Georgia 30602, United States*

Tho Duc Nguyen − *Department of Physics and Astronomy, University of Georgia, Athens, Georgia 30602, United States*

Yiping Zhao − *Department of Physics and Astronomy, University of Georgia, Athens, Georgia 30602, United States;* orcid.org/0000-0002-3710-4159

Complete contact information is available at: https://pubs.acs.org/10.1021/acs.jpcc.0c08057

Notes

The authors declare no competing financial interest.

■ ACKNOWLEDGMENTS

This work was supported by National Science Foundation under Grant no. ECCS-1611330 and ECCS-1808271 (H.M.L. and Y.Z.), the University of Georgia (UGA) startup fund, and STYLENQUAZA LLC.DBA VICOSTONE USA under Award no. AWD00009492 (T.D.N., H.M.L., and M.T.P.). H. M. L. acknowledges funding support from the UGA Graduate School (GRSA).

■ REFERENCES

(1) Shaltout, A. M.; Shalaev, V. M.; Brongersma, M. L. Spatiotemporal light control with active metasurfaces. *Science* **2019**, *364*, No. eaat3100.

(2) Zhang, S.; Zhou, J.; Park, Y.-S.; Rho, J.; Singh, R.; Nam, S.; Azad, A. K.; Chen, H.-T.; Yin, X.; Taylor, A. J.; Zhang, X. Photoinduced handedness switching in terahertz chiral metamolecules. *Nat. Commun.* **2012**, *3*, 942.

(3) Kenanakis, G.; Zhao, R.; Katsarakis, N.; Kafesaki, M.; Soukoulis, C. M.; Economou, E. N. Optically controllable THz chiral metamaterials. *Opt. Express* **2014**, *22*, 12149−12159.

(4) Lv, T. T.; Zhu, Z.; Shi, J. H.; Guan, C. Y.; Wang, Z. P.; Cui, T. J. Optically controlled background-free terahertz switching in chiral metamaterial. *Opt. Lett.* **2014**, *39*, 3066−3069.

(5) Kanda, N.; Konishi, K.; Kuwata-Gonokami, M. All-photoinduced terahertz optical activity. *Opt. Lett.* **2014**, *39*, 3274−3277.

(6) Zhu, Y.; Hu, X.; Chai, Z.; Yang, H.; Gong, Q. Active control of chirality in nonlinear metamaterials. *Appl. Phys. Lett.* **2015**, *106*, 091109.

(7) Kan, T.; Isozaki, A.; Kanda, N.; Nemoto, N.; Konishi, K.; Takahashi, H.; Kuwata-Gonokami, M.; Matsumoto, K.; Shimoyama, I. Enantiomeric switching of chiral metamaterial for terahertz polarization modulation employing vertically deformable MEMS spirals. *Nat. Commun.* **2015**, *6*, 8422.

(8) Wuttig, M.; Yamada, N. Phase-change materials for rewriteable data storage. *Nat. Mater.* **2007**, *6*, 824.

(9) Liu, M.; Hwang, H. Y.; Tao, H.; Strikwerda, A. C.; Fan, K.; Keiser, G. R.; Sternbach, A. J.; West, K. G.; Kittiwatanakul, S.; Lu, J.; Wolf, S. A.; Omenetto, F. G.; Zhang, X.; Nelson, K. A.; Averitt, R. D. Terahertz-field-induced insulator-to-metal transition in vanadium dioxide metamaterial. *Nature* **2012**, *487*, 345.

(10) Wang, Q.; Rogers, E. T. F.; Gholipour, B.; Wang, C.-M.; Yuan, G.; Teng, J.; Zheludev, N. I. Optically reconfigurable metasurfaces and photonic devices based on phase change materials. *Nat. Photonics* **2015**, *10*, 60.

(11) Yin, X.; Schäferling, M.; Michel, A.-K. U.; Tittl, A.; Wuttig, M.; Taubner, T.; Giessen, H. Active Chiral Plasmonics. *Nano Lett.* **2015**, *15*, 4255−4260.

(12) Armelles, G.; Caballero, B.; Prieto, P.; García, F.; Cebollada, A.; González, M. U.; García-Martin, A. Magnetic field modulation of chirooptical effects in magnetoplasmonic structures. *Nanoscale* **2014**, *6*, 3737−3741.

(13) Han, B.; Gao, X.; Shi, L.; Zheng, Y.; Hou, K.; Lv, J.; Guo, J.; Zhang, W.; Tang, Z. Geometry-Modulated Magnetoplasmonic Optical Activity of Au Nanorod-Based Nanostructures. *Nano Lett.* **2017**, *17*, 6083−6089.

(14) Armelles, G.; Cebollada, A.; Feng, H. Y.; García-Martín, A.; Meneses-Rodríguez, D.; Zhao, J.; Giessen, H. Interaction Effects between Magnetic and Chiral Building Blocks: A New Route for Tunable Magneto-chiral Plasmonic Structures. *ACS Photonics* **2015**, *2*, 1272−1277.

(15) Feng, H. Y.; Luo, F.; Arenal, R.; Henrard, L.; García, F.; Armelles, G.; Cebollada, A. Active magnetoplasmonic split-ring/ring nanoantennas. *Nanoscale* **2017**, *9*, 37−44.

(16) Zubritskaya, I.; Maccaferri, N.; Inchausti Ezeiza, X.; Vavassori, P.; Dmitriev, A. Magnetic control of the chiroptical plasmonic surfaces. *Nano Lett.* **2017**, *18*, 302−307.

(17) Armelles, G.; Cebollada, A.; García-Martín, A.; González, M. U. Magnetoplasmonics: Combining Magnetic and Plasmonic Functionalities. *Adv. Opt. Mater.* **2013**, *1*, 10−35.

(18) Luong, H. M.; Pham, M. T.; Ai, B.; Nguyen, T. D.; Zhao, Y. Magnetoplasmonic properties of Ag-Co composite nanohole arrays. *Phys. Rev. B* **2019**, *99*, 224413.

(19) Luong, H. M.; Pham, M. T.; Nguyen, T. D.; Zhao, Y. Magnetoplasmonic properties of Ag-Co composite nano-triangle arrays. *Nanotechnology* **2019**, *30*, 425203.

(20) Ai, B.; Luong, H. M.; Zhao, Y. Chiral Nanohole Arrays. *Nanoscale* **2020**, *12*, 2479−2491.

(21) Larson, S. R.; Luong, H.; Song, C.; Zhao, Y. Dipole Radiation Induced Extraordinary Optical Transmission for Silver Nanorods Covered Silver Nanohole Arrays. *J. Phys. Chem. C* **2019**, *123*, 5634−5641.

(22) Luong, H. M.; Pham, M. T.; Larsen, G. K.; Nguyen, T. D. Plasmonic sensing of hydrogen in Pd nano-hole arrays. *Plasmonics: Des. Mater. Fabr. Char. Appl.* **2019**, *11082*, 110821D.

(23) Luong, H. M.; Pham, M. T.; Madhogaria, R. P.; Phan, M.-H.; Larsen, G. K.; Nguyen, T. D. Bilayer Plasmonic Nano-lattices for Tunable Hydrogen Sensing Platform. *Nano Energy* **2020**, *71*, 104558.

(24) Luong, H. M.; Ai, B.; Zhao, Y.; Nguyen, T. D. Weak enhanced resonant Faraday rotation in pure cobalt plasmonic lattices: Thickness

dependent Faraday rotation studies. *J. Magn. Magn. Mater.* **2018**, *468*, 79−84.
(25) Ebbesen, T. W.; Lezec, H. J.; Ghaemi, H. F.; Thio, T.; Wolff, P. A. Extraordinary optical transmission through sub-wavelength hole arrays. *Nature* **1998**, *391*, 667−669.
(26) FDTD Solutions. https://www.lumerical.com/ (accessed December 26, 2020).
(27) Ingram, W.; He, Y.; Stone, K.; Dennis, W. M.; Ye, D.; Zhao, Y. Tuning the plasmonic properties of silver nanopatterns fabricated by shadow nanosphere lithography. *Nanotechnology* **2016**, *27*, 385301.
(28) Larsen, G. K.; He, Y.; Ingram, W.; Zhao, Y. Hidden chirality in superficially racemic patchy silver films. *Nano Lett.* **2013**, *13*, 6228−6232.
(29) Ohno, T.; Wadell, C.; Inagaki, S.; Shi, J.; Nakamura, Y.; Matsushita, S.; Sannomiya, T. Hole-size tuning and sensing performance of hexagonal plasmonic nanohole arrays. *Opt. Mater. Express* **2016**, *6*, 1594−1603.
(30) Van der Molen, K. L.; Segerink, F. B.; Van Hulst, N. F.; Kuipers, L. Influence of hole size on the extraordinary transmission through subwavelength hole arrays. *Appl. Phys. Lett.* **2004**, *85*, 4316−4318.
(31) Hajiaboli, A.; Kahrizi, M.; Truong, V. V. Optical behaviour of thick gold and silver films with periodic circular nanohole arrays. *J. Phys. D: Appl. Phys.* **2012**, *45*, 485105.
(32) Kim, J. H.; Moyer, P. J. Thickness effects on the optical transmission characteristics of small hole arrays on thin gold films. *Opt. Express* **2006**, *14*, 6595−6603.
(33) Genet, C.; Ebbesen, T. W. Light in tiny holes. *Nature* **2007**, *445*, 39−46.
(34) Degiron, A.; Ebbesen, T. W. The role of localized surface plasmon modes in the enhanced transmission of periodic subwavelength apertures. *J. Optic. Pure Appl. Optic.* **2005**, *7*, S90−S96.
(35) Kondratov, A.; Gorkunov, M.; Darinskii, A.; Gainutdinov, R.; Rogov, O.; Ezhov, A.; Artemov, V. Extreme optical chirality of plasmonic nanohole arrays due to chiral Fano resonance. *Phys. Rev. B* **2016**, *93*, 195418.
(36) Wu, Z.; Zheng, Y. Moiré Chiral Metamaterials. *Adv. Opt. Mater.* **2017**, *5*, 1700034.
(37) Wu, Z.; Chen, X.; Wang, M.; Dong, J.; Zheng, Y. High-performance ultrathin active chiral metamaterials. *ACS Nano* **2018**, *12*, 5030−5041.
(38) Sobhani, A.; Knight, M. W.; Wang, Y.; Zheng, B.; King, N. S.; Brown, L. V.; Fang, Z.; Nordlander, P.; Halas, N. J. Narrowband photodetection in the near-infrared with a plasmon-induced hot electron device. *Nat. Commun.* **2013**, *4*, 1−6.
(39) Martín-Moreno, L.; García-Vidal, F. J.; Lezec, H. J.; Pellerin, K. M.; Thio, T.; Pendry, J. B.; Ebbesen, T. W. Theory of Extraordinary Optical Transmission through Subwavelength Hole Arrays. *Phys. Rev. Lett.* **2001**, *86*, 1114−1117.
(40) Qin, J.; Deng, L.; Kang, T.; Nie, L.; Feng, H.; Wang, H.; Yang, R.; Liang, X.; Tang, T.; Shen, J.; Li, C.; Wang, H.; Luo, Y.; Armelles, G.; Bi, L. Switching the Optical Chirality in Magnetoplasmonic Metasurfaces Using Applied Magnetic Fields. *ACS Nano* **2020**, *14*, 2808−2816.
(41) Luong, H. M.; Pham, M. T.; Nguyen, T. D.; Zhao, Y. Enhanced Resonant Faraday Rotation in Multilayer Magnetoplasmonic Nanohole Arrays and Their Sensing Application. *J. Phys. Chem. C* **2019**, *123*, 28377−28384.

https://dx.doi.org/10.1021/acs.jpcc.0c08057
J. Phys. Chem. C 2021, 125, 716−723